Geometry and symmetry in skyrmion dynamics

Vladyslav M. Kuchkin,[1,2,*] Ksenia Chichay,[3] Bruno Barton-Singer,[4] Filipp N. Rybakov,[5] Stefan Blügel,[1] Bernd J. Schroers,[4] and Nikolai S. Kiselev[1]

[1]*Peter Grünberg Institute and Institute for Advanced Simulation, Forschungszentrum Jülich and JARA, 52425 Jülich, Germany*

[2]*Department of Physics, RWTH Aachen University, 52056 Aachen, Germany*

[3]*Institute of Physics, Mathematics and Information Technology, Immanuel Kant Baltic Federal University, 236041 Kaliningrad, Russia*

[4]*Maxwell Institute for Mathematical Sciences and Department of Mathematics, Heriot-Watt University, Edinburgh EH14 4AS, United Kingdom*

[5]*Department of Physics, KTH Royal Institute of Technology, 10691 Stockholm, Sweden*

(Received 23 April 2021; accepted 22 September 2021; published 8 October 2021)

The uniform motion of chiral magnetic skyrmions induced by a spin-transfer torque displays an intricate dependence on the skyrmions' topological charge and shape. We reveal surprising patterns in this dependence through simulations of the Landau-Lifshitz-Gilbert equation with Zhang-Li torque and explain them through a geometric analysis of Thiele's equation. Our results provide a universal geometrical understanding of the dependence of the skyrmion's velocity and Hall angle on the skyrmion's topological charge, shape, and orientation. The generality of our approach suggests the validity of our results for exchange-frustrated magnets, bubble materials, and other materials.

DOI: 10.1103/PhysRevB.104.165116

I. INTRODUCTION

Skyrmions are examples of topological solitons: stable, particlelike configurations in nonlinear field theories. Originally introduced in the context of nuclear physics by Skyrme [1], the term "skyrmion" is now widely used and has found applications in several distinct areas of physics. This paper is about the dynamics of magnetic skyrmions (Sks) to which we attribute all stable solutions of the static field equations, even when the topological charge is zero.

Since the pioneering works by Bogdanov and coauthors [2–5], both the static and dynamic properties of axisymmetric solutions representing vortexlike spin textures known as $k\pi$-Sks [Fig. 1(a)] have been studied extensively. However, as in the nuclear Skyrme model, removing the assumption of axisymmetry reveals an extraordinary diversity of solutions with arbitrary topological charge. Their static properties have only recently been studied [7–11], and very little is known about their dynamics [12–14].

In the nuclear Skyrme model, understanding static solutions provides only very limited insights into dynamical properties. By contrast, for magnetic Sks the static solutions allow one to deduce interesting features of their dynamics, for instance, in response to an applied current. This fact is explained and exploited in this paper. Drawing on the full range of recently discovered static Sks, we report a striking result: the distribution of the response velocities has a ringlike shape, as shown in Fig. 1(b). We provide a comprehensive analysis of this phenomenon which implies a geometric understanding of the Sk Hall angle valid for any Sk and irrespective of the stabilization mechanism and underlying Hamiltonian.

II. MODEL AND METHODS

Our results are obtained with numerical micromagnetic simulations based on the Landau-Lifshitz-Gilbert equation with Zhang-Li spin-transfer torque (STT) [15] and an analytic method based on the Thiele approach. The latter provides a full mathematical understanding of the ringlike distribution and is confirmed by the former.

We consider the two-dimensional (2D) micromagnetic model for a chiral magnet containing three main energy terms:

$$\mathcal{E} = \int \{w_{\rm ex}(\mathbf{n}) + w_{\rm D}(\mathbf{n}) + w_{\rm U}(\mathbf{n})\}\, l dx dy, \qquad (1)$$

where $\mathbf{n} = \mathbf{M}/M_{\rm s}$ is the magnetization unit vector field uniform across the film thickness l, $M_{\rm s}$ is the saturation magnetization, $w_{\rm ex} = \mathcal{A}|\nabla \mathbf{n}|^2$ is the Heisenberg exchange interaction, and $w_{\rm U} = -M_{\rm s}\mathbf{B}_{\rm ext}\cdot\mathbf{n} - \mathcal{K}n_{\rm z}^2$ is the potential term containing the Zeeman interaction and the easy-axis/easy-plane anisotropy. The external magnetic field is perpendicular to the plane of the film, $\mathbf{B}_{\rm ext} \parallel \mathbf{e}_{\rm z}$.

The Dzyaloshinskii-Moriya interaction (DMI) [16,17] term $w_{\rm D}(\mathbf{n}) = \mathcal{D}w(\mathbf{n})$ is defined by combinations of Lifshitz invariants, $\Lambda_{ij}^{(k)} = n_i\partial_k n_j - n_j\partial_k n_i$. The results presented below are valid for systems with Bloch-type modulations [18] and Néel-type modulations [19–21], as well as for crystals with D_{2d} or S_4 point group symmetry [2]. Without loss of generality, in our calculations we assume Bloch-type DMI where $w(\mathbf{n}) = \Lambda_{zy}^{(x)} + \Lambda_{xz}^{(y)}$. Introducing the characteristic size of chiral modulations $L_{\rm D} = 4\pi\mathcal{A}/\mathcal{D}$ and the characteristic magnetic field $B_{\rm D} = \mathcal{D}^2/(2M_{\rm s}\mathcal{A})$, we reduce the number of independent parameters to two, namely, the dimensionless external magnetic field $h = B_{\rm ext}/B_{\rm D}$ and anisotropy $u = \mathcal{K}/(M_{\rm s}B_{\rm D})$.

The motion of Sks can be caused by different stimuli, e.g., the gradient of the internal or external parameters and

*v.kuchkin@fz-juelich.de

 ©2021 American Physical Society

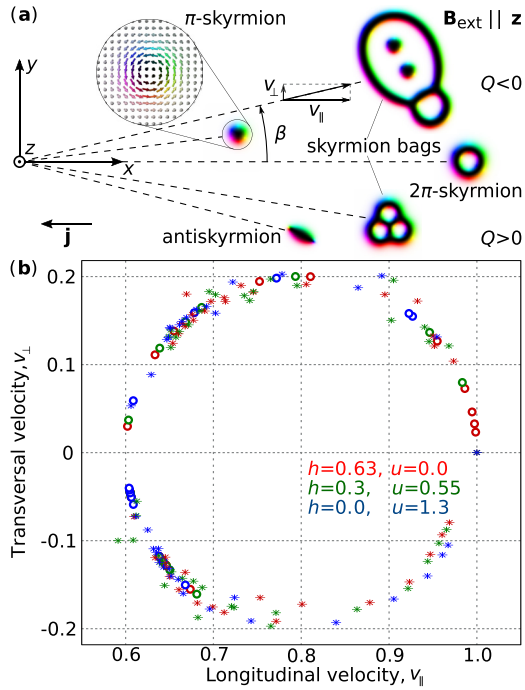

FIG. 1. (a) Schematic representation of the trajectories of chiral Sks moving under electric current $\mathbf{j}$ with skyrmion Hall angle β. The spin texture for π-Sk in the inset explains the color code. The antiskyrmion is provided as an example of a Sk with chiral kinks [10]. (b) The velocity distribution for a wide diversity of Sks obtained in micromagnetic simulations at different values of the external magnetic field h and anisotropy u. The velocities are given in reduced units with respect to the velocity of 2π-Sk. The simulations are performed at realistic values of the Gilbert damping, $\alpha = 0.06$, and the degree of nonadiabaticity, $\xi = 0.1$. The velocities represented by the circle symbols lie on a perfect circle with the center at $v_\parallel = 0.8$, $v_\perp = 0$ irrespective of h and u. The velocities marked by the stretched star symbols lie in close vicinity to that circle. Movie 1 in the Supplemental Material [6] illustrates the steady motion of the skyrmion bag depicted in (a) as a representative example.

spin-orbit or spin-transfer torques [22–25]. Here we consider the particular case of the Zhang-Li STT [15]. The Landau-Lifshitz-Gilbert (LLG) equation [26] in this case has the form

$$\frac{\partial \mathbf{n}}{\partial t} = -\gamma \mathbf{n} \times \mathbf{H}_{\text{eff}} + \alpha \mathbf{n} \times \frac{\partial \mathbf{n}}{\partial t} - \mathbf{T}_{\text{ZL}}, \tag{2}$$

where γ is the gyromagnetic ratio, α is the Gilbert damping, $\mathbf{H}_{\text{eff}} = -\frac{1}{M_s}\frac{\delta \mathcal{E}}{\delta \mathbf{n}}$ is the effective field, and the last term is the Zhang-Li torque:

$$\mathbf{T}_{\text{ZL}} = \mathbf{n} \times [\mathbf{n} \times (\mathbf{I} \cdot \nabla)\mathbf{n}] + \xi\, \mathbf{n} \times (\mathbf{I} \cdot \nabla)\mathbf{n}, \tag{3}$$

where the vector $\mathbf{I} = \mathbf{j}\mu_{\text{B}} p (1+\xi^2)^{-1} (eM_s)^{-1}$ is proportional to the current density $\mathbf{j}$, ξ is the degree of nonadiabaticity [27], p is the polarization of the spin current, μ_{B} is the Bohr magneton, and e is the electron charge.

We study the solutions of Eq. (2) corresponding to uniform motion of magnetic Sks using different values for h and u in our micromagnetic simulations for a large diversity of Sks. The resulting velocity distribution is shown in Fig. 1(b). For details regarding the numerical simulations see Appendixes A–C. To explain the ringlike shape of this distribution we use analytical methods, to which we now turn.

The uniform motion of magnetic textures is well described by Thiele's equation [28], which can be derived from (2) and has the following form [29]:

$$-Q\, \mathbf{e}_z \times (\mathbf{V} + \mathbf{I}) - \Gamma(\alpha \mathbf{V} + \xi \mathbf{I}) = 0, \tag{4}$$

where $\mathbf{V} = (V_x, V_y)^{\text{T}}$ is the velocity vector of the Sk moving as a rigid object, i.e., $\mathbf{n}(\mathbf{r}, t) = \mathbf{n}_0(\mathbf{r} - \mathbf{V}t)$. The two essential parameters in (4) are the topological charge [30]

$$Q = \frac{1}{4\pi} \int \mathbf{n} \cdot (\partial_x \mathbf{n} \times \partial_y \mathbf{n})\, dxdy \tag{5}$$

and the dissipation tensor Γ, whose components are [25,31]

$$\Gamma_{ij} = \frac{1}{4\pi} \int (\partial_i \mathbf{n} \cdot \partial_j \mathbf{n}) dxdy, \quad i, j = x, y. \tag{6}$$

Equation (4) has a simple algebraic form, but to solve it for $\mathbf{V}$ one has to find the Sk profile $\mathbf{n}_0$ [which, in general, should be consistent with the LLG equation (2)] and calculate the integrals in (5) and (6). Previous studies [29,32] showed that for low current density the uniform motion has only a secondary effect on the skyrmion profile. Therefore, the tensor Γ can be calculated with good accuracy from $\mathbf{n}_0$ representing a static equilibrium configuration found by direct energy minimization. This semianalytical approach shows very good agreement with the results of direct micromagnetic simulations based on the LLG equation (2).

Note that we apply the fourth-order finite-difference scheme only to calculate the magnetization spatial derivatives in the Hamiltonian (1) and, consequently, in the effective field term in the LLG equation (2), while magnetization gradients in the STT term in MUMAX are calculated with only second-order accuracy. The latter may lead to small discrepancies between the LLG simulations and Thiele's approach. Nevertheless, in our calculations, the difference never exceeds a few percent when we compare the velocity components.

III. SKYRMION SYMMETRY

As a symmetric and positive 2×2 matrix, Γ can be brought into diagonal form by conjugation with a rotation matrix. In terms of the real eigenvalues $\lambda_1 \geqslant \lambda_2 > 0$ and the rotation angle ψ, we have the parametrization of Γ as

$$\Gamma = R(\psi) \begin{pmatrix} \lambda_1 & 0 \\ 0 & \lambda_2 \end{pmatrix} R(-\psi), \tag{7}$$

where $R(\psi)$ is the 2×2 matrix for a (mathematically positive) rotation by ψ in the plane. The angle ψ is defined as existing only when $\lambda_1 > \lambda_2$ and takes values only in $[0, \pi)$. It parametrizes the unoriented direction of the eigenvector for λ_1 relative to the x axis (see Appendix D). Under the transformation representing the rotation of the whole spin texture about the axis normal to the plane,

$$\mathbf{n}'(\mathbf{r}) = \mathcal{R}(\pm\varphi)\, \mathbf{n}(\mathcal{R}(-\varphi)\mathbf{r}), \tag{8}$$

the angle ψ shifts to $\psi + \varphi$ (see Appendix D). Here $\mathcal{R}(\varphi)$ is the 3×3 matrix for a rotation by φ about the z axis, and the $\pm$ sign depends on the symmetry of the Lifshitz invariant used.

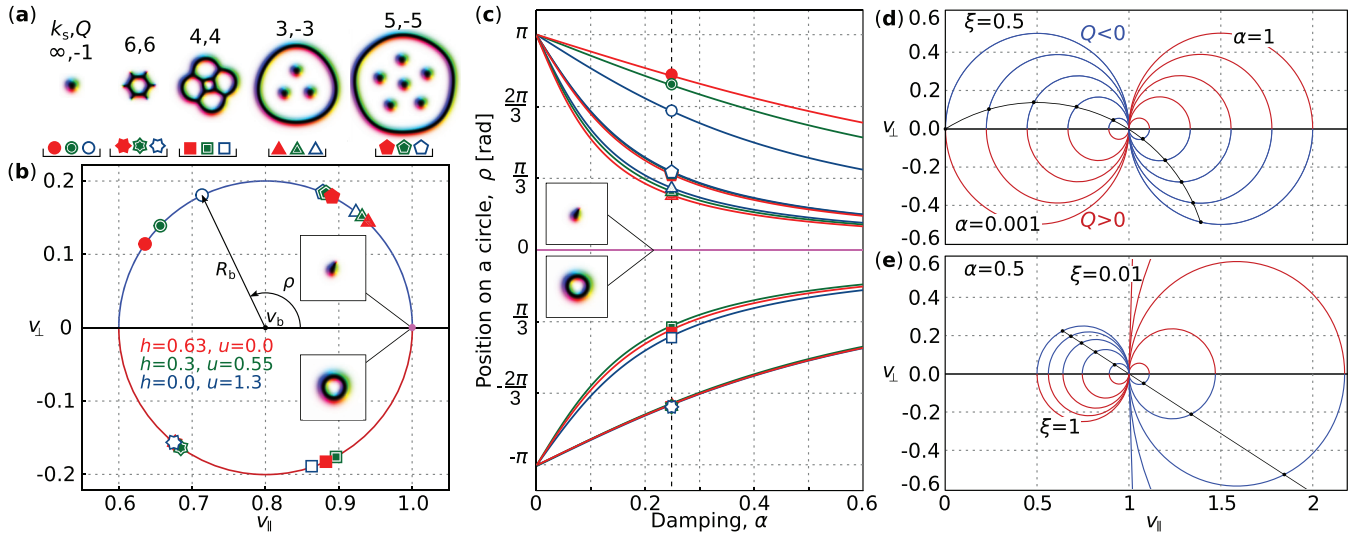

FIG. 2. (a) The set of representative HSSks with different orders of the rotational symmetry k_s and topological charge Q. (b) The velocities of Sks depicted in (a), calculated with the semianalytical approach for Gilbert damping $\alpha = 1/4$, degree of nonadiabaticity $\xi/\alpha = 5/3$, and various values of h and u, as indicated by the different colors. The velocity of topologically trivial solutions, e.g., the chiral droplet and 2π-Sk (see insets), is marked by a magenta circle, $v_\parallel = 1$, $v_\perp = 0$. Red and blue half circles correspond to $Q > 0$ and $Q < 0$, respectively. (c) The change in the distribution of velocities on the circle in terms of angle ρ for the solitons depicted in (a) as a function of $\alpha \in (0, 0.6]$ for fixed $\xi/\alpha = 5/3$. The dashed line corresponds to damping parameter $\alpha = 1/4$ as in (b). (d) The transformation of the circle (11) under varying α at fixed $\xi = 0.5$. The circles correspond to α in the interval $[0.001, 1]$ with $\Delta\alpha = 0.111$. (e) The transformation of the circle (11) at fixed $\alpha = 0.5$ and ξ varying in the interval $[0.01, 1]$ with $\Delta\xi = 0.11$. Black dots in (a) and (b) are the velocities of ordinary π-Sk.

The transformation (8) represents a zero-energy mode for the Hamiltonian (1) and can be used to define the rotational symmetry of Sks. When the transformation (8) with $\varphi = 2\pi/k$ is trivial for some positive integers k, so that $\mathbf{n}' = \mathbf{n}$, we say that Sk has a rotational symmetry of order $k_s = \max(k)$. For axially symmetric Sks the invariance holds for any k, and we write $k_s = \infty$ [Fig. 2(a)].

IV. GEOMETRY OF THE THIELE EQUATION

To reveal the geometry in Thiele's equation, we introduce the parameters

$$\rho = 2\tan^{-1}\left(\frac{-Q}{\alpha\sqrt{\lambda_1\lambda_2}}\right), \quad \vartheta = \ln\sqrt{\frac{\lambda_1}{\lambda_2}} \tag{9}$$

and write the general solution of (4) in an orthonormal basis $(\mathbf{e}_\parallel, \mathbf{e}_\perp)$, where $\mathbf{e}_\parallel$ is antiparallel to $\mathbf{j}$, as

$$\mathbf{v} = \mathbf{V}/V_0 = (v_b + R_b\cos\rho)\mathbf{e}_\parallel + R_b\sin\rho[\cosh\vartheta - \sinh\vartheta\, R(2\psi)P]\mathbf{e}_\perp, \tag{10}$$

where $V_0 = \xi|\mathbf{I}|/\alpha$ is the speed of the skyrmionium [29], P is the matrix for the reflection on the x axis, and the parameters $v_b = \frac{1}{2}(\xi + \alpha)/\xi$ and $R_b = \frac{1}{2}(\xi - \alpha)/\xi$ are determined by the Gilbert damping and the degree of nonadiabaticity. For the derivation of (10) and a general discussion of its geometry, see Appendixes E and F. The parameter ρ vanishes for any Sk with $Q = 0$, while necessarily $\vartheta = 0$ ($\lambda_1 = \lambda_2$) for Sks with $k_s > 2$ (see Appendix D). These facts motivate splitting all Sks into three classes: *topologically trivial* Sks (TTSks) with $Q = 0$, *high-symmetry* Sks (HSSks) with $k_s > 2$, and *low-symmetry* Sks (LSSks) with $k_s = 1$ or 2.

Formula (10) captures the geometry referred to in the title and provides the key to understanding the ringlike velocity distribution depicted in Fig. 1(b). For TTSks, the velocity takes the single value $\mathbf{v} = \mathbf{e}_\parallel$, regardless of k_s. The velocities of HSSks with $\vartheta = 0$ but different values of ρ lie on a circle with radius R_b and center $v_b\mathbf{e}_\parallel$ (Fig. 2). In terms of the components of $\mathbf{v}$ with respect to the basis $(\mathbf{e}_\parallel, \mathbf{e}_\perp)$, we have

$$\lambda_1 = \lambda_2 \Rightarrow (v_\parallel - v_b)^2 + v_\perp^2 = R_b^2. \tag{11}$$

For fixed ξ/α, irrespective of the external magnetic field h and anisotropy u, which significantly change the shape and size of the Sks (Fig. S3(a) in the Supplemental Material [6]), the velocities of all HSSks are restricted to the same circle (11). Figure 2(b) illustrates the physical meaning of the parameter ρ, which defines the position of a HSSk on the circle. The angle ρ is linked to the experimentally measurable Sk Hall angle [25] $\beta = \arctan(v_\perp/v_\parallel)$ via

$$\tan\beta = \frac{\sin\rho\sin\beta_{\max}}{1 + \cos\rho\sin\beta_{\max}}, \tag{12}$$

where $\beta_{\max} = \arcsin(R_b/v_b)$ is the maximal Sk Hall angle for HSSks. This provides the promised geometrical interpretation of the Hall angle for HSSk. The velocities of HSSks with $Q < 0$ and $Q > 0$ occupy half of the circle in the upper or lower half plane depending on $\mathrm{sgn}(\xi - \alpha)$ [Figs. 2(d) and 2(e)]. When $\xi = \alpha$, the velocity circle degenerates into a single point, meaning that all Sks move with the same velocity $\mathbf{V}_0 = V_0\mathbf{e}_\parallel$. The sign for the Sk Hall angle is inverted for the cases $\xi < \alpha$ and $\xi > \alpha$, both experimentally achievable [33].

Rotating a LSSk with given $\vartheta > 0$ ($\lambda_1 > \lambda_2$) and a given value of ρ according to (8) generates a family of configurations with the same energy but with different spatial

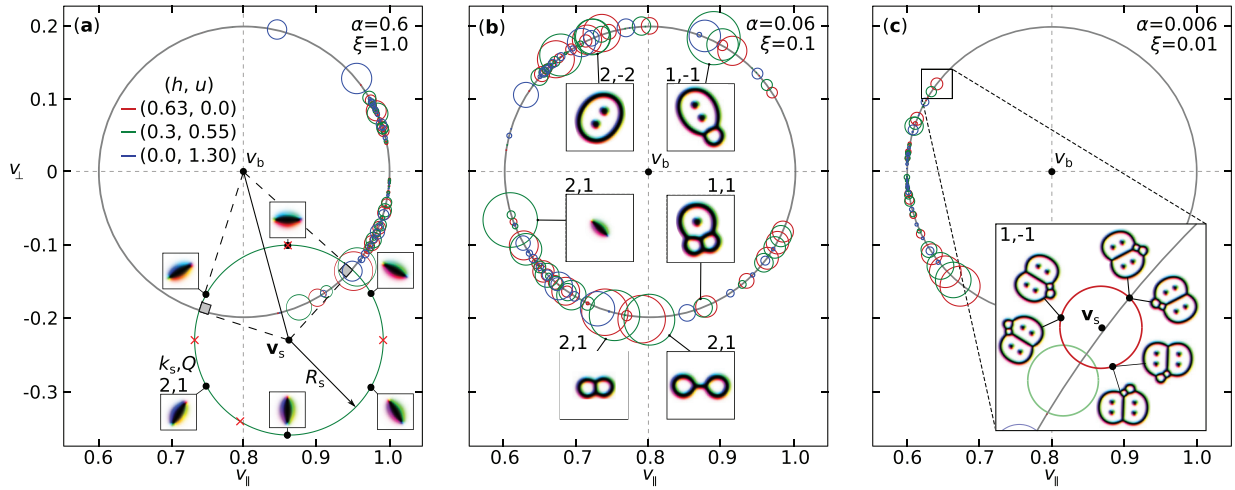

FIG. 3. (a)–(c)The velocity distributions for various low-symmetry Sks at different α and ξ. Some Sks are depicted in the insets. The gray velocity circle for high-symmetry Sks (2) is provided for comparison. The velocity of low-symmetry Sks depends on the rotation angle of the Sk with respect to the current and forms an individual circle for each low-symmetry Sk, as illustrated for the antiskyrmion with $k_s = 2$ in (a) and another low-symmetry Sk with $k_s = 1$ in (c). For the orientations marked with red crosses on the circle for the antiskyrmion in (a) Movie 2 in the Supplemental Material illustrates the soliton motion with constant orientation relative to the current, obtained in micromagnetic simulations [6].

orientations, parametrized by the angle ψ. In our simulations we find that, after an initial transient stage, this orientation does not change when the LSSk is subjected to a Zhang-Li STT. Movie 1 in the Supplemental Material illustrates this fact for the skyrmion with $k_s = 1$ and $Q = -1$ depicted in Fig. 1(a) and in the inset in Fig. 3(b). However, the steady-state response velocity itself *does* depend on the orientation and sweeps out a circle as ψ varies. Movie 2 in the Supplemental Material shows the steady motion of the antiskyrmion depicted in Fig. 3(a) for different orientations relative to the current direction indicated by red crosses on the corresponding circle [6]. For any LSSk, this circle is traversed twice when we rotate the configuration through 2π; it has center coordinates

$$\mathbf{v}_s = (v_{s,\parallel}, v_{s,\perp}) = (v_b + R_b \cos\rho, R_b \sin\rho \cosh\vartheta) \quad (13)$$

and radius

$$R_s = R_b |\sin\rho| \sinh\vartheta = R_b \frac{\alpha|Q|(\lambda_1 - \lambda_2)}{\alpha^2\lambda_1\lambda_2 + Q^2}. \quad (14)$$

These circles tend to have radii, R_s, smaller than R_b, so we refer to them as small circles in the following. The centers of the small circles are generally close to the big circle (11), so their collective effect is to generate the ringlike distribution which we see in Fig. 1(b). As follows from (13) and (14), the radius of a small circle and the position of its center are linked to the parameters of the big circle via $(v_{s,\parallel} - v_b)^2 + (v_{s,\perp})^2 = R_b^2 + R_s^2$, which implies that (i) any small circle and the big circle intersect at right angles [Fig. 3(a)] and (ii) the position of the center of any small circle is always outside the big circle and approaches it with decreasing R_s. In the limit $R_s \to 0$, small circles degenerate into points on the big circle.

For LSSks, the velocity formula (10) has an interesting dependence on the Sk orientation, which was previously observed in the context of systems with frustrated exchange interactions [34]. It also implies a universal expression for the Sk Hall angle which generalizes (12) for LSSks irrespective of the underlying Hamiltonian and Sk stabilization mechanism. We discuss the general formula and the orientational dependence further in Appendix F.

We observe that the velocity of topologically nontrivial Sks depends on α and ξ in rather different ways. We illustrate this for the case of π-Sks using red circles in Figs. 2(d) and 2(e), respectively. When α is constant, the trace of $(v_\parallel(\xi), v_\perp(\xi))$ is a straight line, while keeping ξ constant but varying α produces yet another circle,

$$\left(v_\parallel - \frac{1}{2}\right)^2 + \left(v_\perp - \frac{Q}{2\lambda\xi}\right)^2 = \frac{1}{4}\left(1 + \frac{Q^2}{\lambda^2\xi^2}\right), \quad (15)$$

where $\lambda = \lambda_1 = \lambda_2$.

It is natural to ask which Sks move the fastest at fixed dynamical parameters (I, α, ξ). For $\alpha < \xi$, TTSks move with speed $v = 1$, bounding the speed of HSSks. However, LSSks can exceed this speed if the radius R_s (14) is sufficiently large and the Sk has a suitable orientation. Since R_s is directly proportional to the difference $\lambda_1 - \lambda_2$ of the eigenvalues of the dissipation tensor, elongated Sks with $\lambda_1 \gg \lambda_2$ are good candidates for high-speed motion. For the antiskyrmion, λ_1/λ_2 is of order 5; according to Thiele's equation, its speed can exceed $v = 1$. This is illustrated in Fig. 3(a) and confirmed by numerical simulations of the LLG equation. Furthermore, it follows from (F1) that, when $\lambda_1 - \lambda_2 > 2|Q|/\alpha$, the longitudinal component of the LSSk velocity $v_\parallel$ exceeds 1 for a suitably chosen orientation. For instance, for $\alpha = 0.9$, $\xi = 1.5$, $h = 0.3$, and $u = 0.55$, the antiskyrmion satisfies this condition and can travel with $v_\parallel > 1$. Therefore, contrary to what one might deduce from Fig. 3(a), the longitudinal velocity of the TTSk can be exceeded by that of LSSks which satisfy the condition above.

V. CONCLUSIONS

We showed that the Sk velocity distribution can be understood by splitting all Sks into high-symmetry, low-symmetry,

and topologically trivial ones. Irrespective of the magnetic field and anisotropy, the velocities of high-symmetry Sks all lie on the circle (11). The radius R_b of that circle depends exclusively on the current density $\mathbf{j}$, Gilbert damping α, and the coefficient of nonadiabaticity of the electric current ξ. The low-symmetry Sks exhibit an even more intriguing behavior: their velocities depend on the Sk orientation with respect to the current direction, and when we vary the orientation for a given Sk, the velocities sweep out a circle with a radius which is generally smaller than R_b. The combination of small circles near the big circle (11) produces the ringlike distribution [Fig. 1(b)]. The variation of α and ξ can lead to the degeneration of all those circles into one point when all Sks move along one trajectory with the same velocity.

Due to the generality of our approach, the presented results are valid not only for chiral magnets of various symmetries but also for frustrated magnets and bubble domain materials (see Appendix G).

ACKNOWLEDGMENTS

The authors acknowledge financial support from the European Research Council (ERC) under the European Union's Horizon 2020 research and innovation program (Grant No. 856538, project "3D MAGiC"), Deutsche Forschungsgemeinschaft (DFG) through SPP 2137 "Skyrmionic" Grants No. KI 2078/1-1 and No. SB 444/16. B.B.-S. acknowledges an EPSRC-funded Ph.D. studentship. F.N.R. acknowledges support from Swedish Research Council Grants No. 642-2013-7837, No. 2016-06122, and No. 2018-03659 and the Göran Gustafsson Foundation for Research in Natural Sciences.

APPENDIX A: MICROMAGNETIC SIMULATIONS

Micromagnetic simulations were performed with the MUMAX code [35] on a rectangular domain with shape $L_x \times L_y$ with periodic boundary conditions (PBCs). In general, the interaction between the skyrmion instances because of PBCs may change the dynamics of the skyrmions. This effect becomes especially pronounced when the domain of simulation is so small that it affects the shape and thus the symmetry of the skyrmion. To diminish this effect as much as possible we use large size domains, $L_x, L_y \sim 10L_D$.

To improve the accuracy in the LLG simulations, instead of the second-order finite-difference scheme used by default in MUMAX, we implemented a fourth-order scheme in the spirit of the approach suggested by Donahue and McMichael [36]. For details, see Appendix B, where we discuss various aspects of the accuracy in micromagnetic simulations, and Appendix C, where we provide the MUMAX script with the fourth-order finite-difference scheme implemented.

The skyrmion position can be traced using the approach suggested in Ref. [37], which is based on the formula for the center of mass of a nonuniform rod, but with the topological density—the integrand in Eq. (5) or magnon density [38] as in Ref. [29]—playing the role of distributed mass. In long-time dynamics, when the skyrmion can cross the boundary of the simulated domain with PBCs multiple times, this approach needs to be adapted. In particular, when the skyrmion comes near the boundary of the simulation domain and part of it appears on the opposite side of the simulated domain, this formula suggests that the skyrmion slows down and starts to move in the opposite direction. We suggest an alternative approach to calculate the center of the skyrmion, which follows from the solution of the problem for the center of mass of a nonuniform ring. The skyrmion position, (x_p, y_p) can be defined as follows:

$$x_p = \frac{L_x}{2\pi} \tan^{-1} \frac{\int \mathcal{N}_y \sin(2\pi x/L_x) dx}{\int \mathcal{N}_y \cos(2\pi x/L_x) dx} + l_x L_x, \tag{A1}$$

$$y_p = \frac{L_y}{2\pi} \tan^{-1} \frac{\int \mathcal{N}_x \sin(2\pi y/L_y) dy}{\int \mathcal{N}_x \cos(2\pi y/L_y) dy} \pm l_y L_y, \tag{A2}$$

where $\mathcal{N}_x \equiv \mathcal{N}_x(y) = \int (1 - n_z) dx$ and $\mathcal{N}_y \equiv \mathcal{N}_y(x) = \int (1 - n_z) dy$ are the magnon densities averaged along x and y, respectively. The integer numbers l_x and l_y indicate how many times the skyrmion has crossed the domain boundary in the x and y directions, respectively. The sign in front of l_y depends on whether the skyrmion crosses the boundary in the positive or negative direction of the corresponding axis, which in turn depends on the sign for the deflection angle β. Since, in our setup [Fig. 1(a)], the skyrmions move along the positive x axis, the sign in front of l_x is always positive. The approach to trace the position of the soliton presented here is similar to that for calculating the center of mass for a set of point masses that are distributed in the unbounded 2D environment presented in Ref. [39].

The initial spin configurations for various types of skyrmions were either manually crafted according to the method described in Ref. [7] or constructed through analytical functions as in Ref. [10].

APPENDIX B: ACCURACY OF MICROMAGNETIC SIMULATIONS

Insufficient accuracy in the numerical calculation of the magnetization spatial derivatives with finite-difference schemes may lead to artifacts in micromagnetic simulations and provide misleading or inconsistent results. This becomes especially important for skyrmions with a complex shape and large size. In Ref. [7] we showed that the second-order finite-difference scheme often used in micromagnetic calculations may lead to significant discrepancies with the exact solution even when quite dense meshes with ~100 nodes per L_D are used. There, we also showed that the accuracy of energy calculations can be improved approximately by an order of magnitude in the case of the fourth-order scheme [36]. We found that in the case of LLG dynamics, the second-order scheme may provide artifacts that one can get rid of by employing a fourth-order discretization scheme. For better consistency of LLG simulations and numerical solutions of Thiele's equation it is also advisable to use the fourth-order discretization scheme in the numerical calculations of integrals (6).

Two representative examples of the artifacts occur due to insufficient accuracy in the numerical calculations. The first one is the nonzero deflection angle of topologically trivial skyrmions. According to the general solution of Thiele's equation [see Eq. (10)], for $Q = 0$ (so $\rho = 0$), the component of

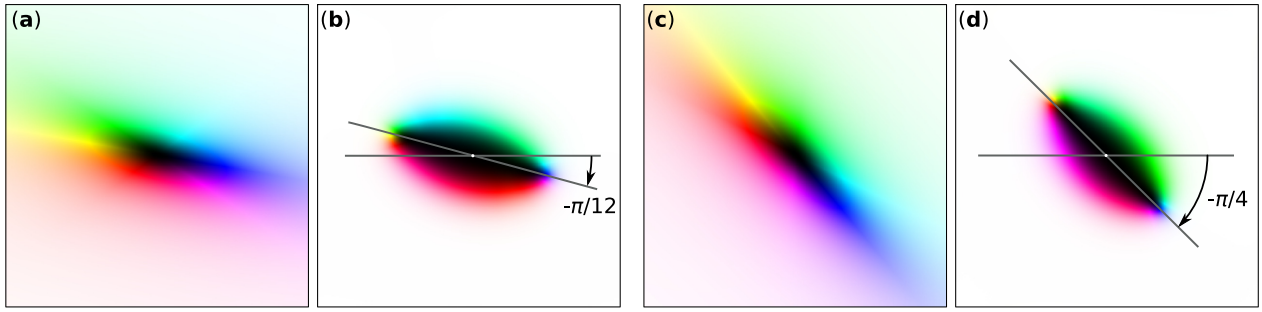

FIG. 4. (a) The initial configuration for an antiskyrmion with the rotation by $\varphi = -\pi/12$ and (b) the corresponding state after energy minimization. (c) and (d) The initial and relaxed states for an antiskyrmion with $\varphi = -\pi/4$. See Movie 2 in the Supplemental Material for steady motion of antiskyrmions with different φ.

the soliton velocity transverse to the current must be zero irrespective of soliton symmetry [see, e.g., the skyrmionium and chiral droplet in Fig. 2(b)]. An axisymmetric soliton, for instance, skyrmionium, may lose its axial symmetry while in steady motion [29]. Nevertheless, in the case of $Q = 0$, after the transient stage is over and the skyrmion speed reaches saturation, its transverse velocity component must be zero. The nonzero transverse component of the velocity for solitons with $Q = 0$ indicates either inaccuracy of the numerical scheme or that the instantaneous velocity is estimated before steady-state motion is reached [12,40–43]. One can use the steady motion of topologically trivial solitons without deflection to test numerical scheme accuracy.

Another artifact which can be observed in LLG simulations is the rotation of the soliton with respect to its initial state at $t = 0$. With the second-order finite-difference scheme, low-symmetry skyrmions, during the transient state or even during the initial energy minimization, rotate such that their long axis coincides with one of the diagonals of the underlying rectangular mesh (see Fig. 4). A high mesh density and the fourth-order finite-difference scheme eliminate this effect and make the behavior of the solitons consistent with the general solution of Thiele's equation (10).

APPENDIX C: MUMAX SCRIPT

```
/*Mumax script with the fourth-order finite difference scheme implemented for 2D with PBC*/
h := 0.3                // [ ] dimensionless external magnetic field
u := 0.55               // [ ] dimensionless anisotropy
/************************************* Material constants ******************************/
LD := 128.0e-9          // [ nm ]
Ms := 384e3             // [ A/m ]
A := 4.0e-12            // [ J/m ]
D := 4.0 * pi * A / LD  // [ J/m^2 ]
BD := D*D/(2*A*Ms)      // [ T ]
B := h*BD               // [ T ]
K := u*D*D/(2*A)        // [ J/m^3 ]
Ku1 = K                 // [ J/m^3 ]
B_ext = vector(0,0,B)   // [ T ] External field vector
anisU = vector(0, 0, 1) // [ ] Anisotropy unit vector
/********************************** Sets GridSize, CellSize and PBC ***********************/
nx := 256; ny := 256; nz := 1;
Lx := 2*LD; Ly := Lx; Lz := 1e-9;
dx := Lx/nx; dy := Ly/ny; dz := Lz/nz;
SetMesh(nx, ny, nz, dx, dy, dz, 1, 1, 0);
/************************************ Initial state, see Ref. [9] ***********************/
l := 60; //size of Ask
f := -pi/12; //rotation angle with respect to initial configuration
for ix:=0; ix<nx; ix++ {
 for iy:=0; iy<ny; iy++ {
  rx := (ix - 0.5*nx)*Lx/LD;
  ry := (iy - 0.5*ny)*Ly/LD;
  rxp := (rx*cos(f-pi/4) + ry*sin(f-pi/4))/l;
  ryp := (ry*cos(f-pi/4) - rx*sin(f-pi/4))/l;
  gm := 5*(rxp*rxp + ryp*ryp)/4 - 2*rxp*ryp -1;
```

```
  gp := 1/(5*(rxp*rxp + ryp*ryp)/4 - 2*rxp*ryp +1);
  m1 := gp*(2*rxp - ryp);
  m2 := gp*(rxp - 2*ryp);
  m3 := gp*gm;
  mnew:=vector(m1*cos(f-pi/4)-m2*sin(f-pi/4), m2*cos(f-pi/4)+m1*sin(f-pi/4), m3);
  m.SetCell(ix, iy, 0, mnew);
 }
}
save(m)           // see Fig. 4 a and c
/************************************ The 2th order scheme ****************************/
// Msat = Ms
// Aex = A
// Dbulk = D
/************************************ The 4th order scheme ****************************/
Msat = Ms
Aex = A*(4/3) // Exchange constant for nearest neighbor
Dbulk = D*(4/3) // DMI constant for nearest neighbor
/************************************ Fourth order Exchange ***************************/
NewAex:= A*(-1/12)
prefactorXA := Const( (2 * NewAex) / (dx*dx*Msat.Average()))
prefactorYA := Const( (2 * NewAex) / (dy*dy*Msat.Average()))
prefactorZA := Const( (2 * NewAex) / (dz*dz*Msat.Average()))
/************************************ Next-nearest-neighbor-X *************************/
left := Mul(Add(Mul(Const(-1),m),Shifted(m, 2, 0, 0)),Shifted(Const(1), 2, 0, 0))
left = Add(left, Mul(Add(Mul(Const(-1),m),Shifted(m,2-nx,0,0)),Shifted(Const(1),2-nx,0,0)))
/************************************ Next-nearest-neighbor+X *************************/
right:= Mul(Add(Mul(Const(-1),m),Shifted(m, -2, 0, 0)),Shifted(Const(1), -2, 0, 0))
right = Add(right,Mul(Add(Mul(Const(-1),m),Shifted(m,nx-2,0,0)),Shifted(Const(1),nx-2,0,0)))
/************************************ Next-nearest-neighbor-Y *************************/
backward:= Mul(Add(Mul(Const(-1),m),Shifted(m, 0, 2, 0)),Shifted(Const(1), 0, 2, 0))
backward = Add(backward,Mul(Add(Mul(Const(-1),m),Shifted(m,0,2-ny,0)),Shifted(Const(1),
  0,2-ny,0)))
/************************************ Next-nearest-neighbor+Y *************************/
forward:= Mul(Add(Mul(Const(-1),m),Shifted(m, 0, -2, 0)),Shifted(Const(1), 0, -2, 0))
forward = Add(forward, Mul(Add(Mul(Const(-1),m),Shifted(m,0,nx-2,0)),Shifted(Const(1),
  0,nx-2,0)))
leftA := Mul(prefactorXA,left)
rightA := Mul(prefactorXA,right)
forwardA := Mul(prefactorYA,forward)
backwardA := Mul(prefactorYA,backward)
/************************ Exchange custom effective field next-nearest-neighbor ***********/
BcA := Add(leftA,Add(rightA,Add(forwardA,backwardA)))
AddFieldTerm(BcA)
addEdensTerm(Mul(Const(-0.5),Dot(BcA,M_full)))
/************************************ Fourth order DMI ********************************/
NewD:= D*(-1/6)
prefactorXD := Const( (2 * NewD) / (2*dx*Msat.Average()))
prefactorYD := Const( (2 * NewD) / (2*dy*Msat.Average()))
prefactorZD := Const( (2 * NewD) / (2*dz*Msat.Average()))
/************************************ Next-nearest-neighbor X*************************/
overx := Mul(prefactorXD,Add(Cross(left,constVector(-1,0,0)),Cross(right,constVector(1,0,0))))
/************************************ Next-nearest-neighbor Y*************************/
overy := Mul(prefactorYD, Add(Cross(backward,constVector(0,-1,0)),Cross(forward,
  constVector(0,1,0))))
/************************** DMI custom effective field next-nearest-neighbor **********/
BcDMI := Add( overx, overy ) AddFieldTerm(BcDMI) addEdensTerm(Mul(Const(-0.5),Dot(BcDMI,M_full)))
```

```
/****************************************** Relax initial state ***************************/
TableAdd(Edens_total)
EnableDemag = false
relax()
minimize()
TableSave()
save(m)                  // see Figs. 4b and 4d
alpha = 0.06             // [ ] Gilbert damping
/************************************* Electric current parameters ********************/
hb:= 1.054571817e-34  // [ J*s ] Planck constant h-bar, h/(2*pi)
em:= 9.1093837015e-31 // [ kg ] the electron rest mass
Pol = 1.0             // [ ] electric current polarization
xi = 0.1              // [ ] the degree of non-adiabaticity
jx:= 5e9              // [A/m^2] electric current density
j = vector(-jx, 0, 0) // [A/m^2] vector along the negative x-axis
I:= hb/(2*em)*jx*Pol.Average()/Ms/(1+xi.Average()*xi.Average())
print(''I='',I)       // print the value of electric current parameter, I
/********************************************* Run simulation ***************************/
t_total := 100e-9    // [ s ]
tableautosave(1e-12)  // [ s ]
autosave( m, 10e-11)  // [ s ]
run(t_total)
```

APPENDIX D: SKYRMION ROTATION AND DISSIPATION TENSOR

The skyrmions possessing rotational symmetry of order $k_s > 2$ have the property that the response velocity determined by Thiele's equation (4) is invariant under the rotation (8) of a skyrmion by an arbitrary angle φ, while for skyrmions with $k_s = 1$ or 2, the response velocity in general depends on the rotation angle. This statement can be proven as follows. Inserting (8) into (5) and (6), one can show that for any configuration localized in space, the topological charge Q is invariant under such rotations. On other hand, the dissipation tensor transforms according to $\Gamma' = R(\varphi)\,\Gamma\,R(-\varphi)$, where $R(\varphi)$ is the 2×2 matrix for a (mathematically positive) rotation by φ in the plane (Fig. 5). This transformation law has the more convenient representation

$$\mathbf{S}' = R(2\varphi)\mathbf{S}, \tag{D1}$$

where $\mathbf{S}$ is a 2D vector, $\mathbf{S} = (\Gamma_{xx} - \Gamma_{yy},\ 2\Gamma_{xy})^{\mathrm{T}}$. If the spin texture is invariant under rotations by angles $\varphi = 2\pi/k_s$ ($\mathbf{n}' = \mathbf{n}$), it follows that $\Gamma' = \Gamma$ and $\mathbf{S}' = \mathbf{S}$ for those angles. For skyrmions with $k_s = 1$ or 2, this condition is satisfied automatically since $R(4\pi/k_s)$ is the identity matrix, $R = \mathrm{id}$. For such spin configurations, the components of the vector $\mathbf{S}$ and Γ tensor may, strictly speaking, take any value. For skyrmions with rotational symmetry $k_s > 2$, on the other hand, it follows that $\mathbf{S}$ must be a zero vector, and thus, $\Gamma_{xx} = \Gamma_{yy}$, $\Gamma_{xy} = 0$, meaning that Γ is proportional to an identity matrix, $\Gamma = \frac{1}{2}(\Gamma_{xx} + \Gamma_{yy})\,\mathrm{id} = \frac{1}{2}\mathrm{Tr}(\Gamma)\,\mathrm{id}$. It follows from (D1) that for such skyrmions the dissipation tensor and, as a result, the velocities determined by Thiele's equation (4) are, indeed, invariant under rotations (8) by an arbitrary angle φ. Motivated by this proof, we distinguish topologically nontrivial skyrmions by their symmetry. We refer to skyrmions with $k_s = 1$ or 2 as *low-symmetry skyrmions* and to skyrmions with $k_s > 2$ as *high-symmetry skyrmions*.

APPENDIX E: THIELE'S EQUATION AND ITS GENERAL SOLUTION

To derive the general solution (10) of Thiele's equation (4) we use the abbreviation

$$\Omega = \begin{pmatrix} 0 & -1 \\ 1 & 0 \end{pmatrix}$$

for the $\pi/2$ rotation in the plane and write Thiele's equation as

$$\left(\Gamma + \frac{Q}{\alpha}\Omega\right)\mathbf{V} = \left(\Gamma + \frac{Q}{\xi}\Omega\right)\left(-\frac{\xi}{\alpha}\mathbf{I}\right). \tag{E1}$$

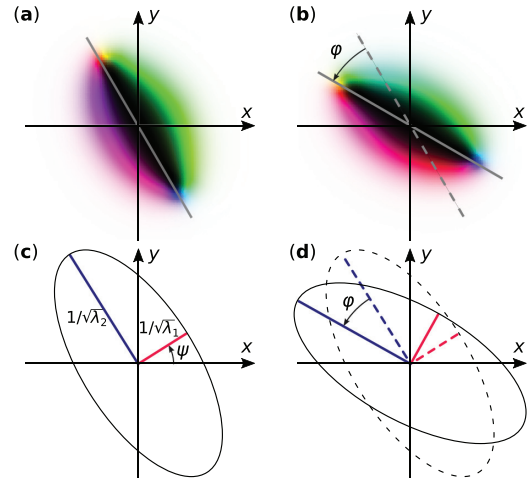

FIG. 5. Illustration of the rotational zero-energy mode. The spin texture of an antiskyrmion (a) before and (b) after the rotation by an angle φ according to (8). The spin textures in (a) and (b) are represented by the standard color code explained in Fig. 1(a). The ellipses in (c) and (d) are the geometrical representations of a 2×2 matrix of Γ computed for the spin textures depicted in (a) and (b), respectively.

Starting with the elementary observation that

$$\Gamma + \frac{Q}{\xi}\Omega = \frac{\xi+\alpha}{2\xi}\Big(\Gamma + \frac{Q}{\alpha}\Omega\Big) + \frac{\xi-\alpha}{2\xi}\Big(\Gamma - \frac{Q}{\alpha}\Omega\Big),$$

we deduce

$$\Big(\Gamma + \frac{Q}{\alpha}\Omega\Big)^{-1}\Big(\Gamma + \frac{Q}{\xi}\Omega\Big) = \frac{\xi+\alpha}{2\xi} + \frac{\xi-\alpha}{2\xi}\Big(\Gamma + \frac{Q}{\alpha}\Omega\Big)^{-1}\Big(\Gamma - \frac{Q}{\alpha}\Omega\Big).$$

With $\vartheta = \ln\sqrt{\lambda_1/\lambda_2}$ as in the main text, we introduce the diagonal matrix

$$D(\vartheta) = \begin{pmatrix} e^{\vartheta} & 0 \\ 0 & e^{-\vartheta} \end{pmatrix}$$

and the rotation matrix

$$R(\varphi) = \begin{pmatrix} \cos\varphi & -\sin\varphi \\ \sin\varphi & \cos\varphi \end{pmatrix}$$

to write the dissipation tensor as

$$\Gamma = R(\psi)\begin{pmatrix} \lambda_1 & 0 \\ 0 & \lambda_2 \end{pmatrix}R(-\psi) = \sqrt{\lambda_1\lambda_2}R(\psi)D(\vartheta)R(-\psi).$$

Then we deduce, with $\tan\frac{\rho}{2} = -\frac{Q}{\alpha\sqrt{\lambda_1\lambda_2}}$ as in the main text, that

$$\Big(\Gamma + \frac{Q}{\alpha}\Omega\Big)^{-1}\Big(\Gamma - \frac{Q}{\alpha}\Omega\Big) = R(\psi)\Big(\Omega^{-1}D(\vartheta) - \tan\frac{\rho}{2}\Big)^{-1} \times \Big(\Omega^{-1}D(\vartheta) + \tan\frac{\rho}{2}\Big)R(-\psi).$$

Noting that $\Omega^{-1}D(\vartheta)\Omega^{-1}D(\vartheta) = -1$ implies

$$\cos^2\frac{\rho}{2}\Big(\Omega^{-1}D(\vartheta) - \tan\frac{\rho}{2}\Big)\Big(\Omega^{-1}D(\vartheta) + \tan\frac{\rho}{2}\Big) = -1$$

and using trigonometric identities, we conclude

$$\Big(\Gamma + \frac{Q}{\alpha}\Omega\Big)^{-1}\Big(\Gamma - \frac{Q}{\alpha}\Omega\Big) = \cos\rho + \sin\rho\,\Omega R(\psi)D(\vartheta)R(-\psi).$$

Now multiplying out matrices and using the matrix

$$P = \begin{pmatrix} 1 & 0 \\ 0 & -1 \end{pmatrix}$$

for the reflection on the x axis, we arrive at the expression

$$\Big(\Gamma + \frac{Q}{\alpha}\Omega\Big)^{-1}\Big(\Gamma - \frac{Q}{\alpha}\Omega\Big) = \cos\rho + \sin\rho\,\Omega[\cosh\vartheta\,\mathrm{id} + \sinh\vartheta R(2\psi)P].$$

Using this to solve (E1) for $\mathbf{V}$, switching to $\mathbf{v}$, and expressing it in terms of the orthonormal basis $(\mathbf{e}_\parallel, \mathbf{e}_\perp)$ and the circle parameters v_b and R_b, one arrives at formula (10).

APPENDIX F: GEOMETRY IN VELOCITY SPACE

We prove the geometrical results related to circles and ellipses in velocity space stated in the main text. We write $P_\psi = R(2\psi)P = R(\psi)PR(-\psi)$ for the reflection on the line with polar angle ψ. Denoting the polar coordinate of the direction $\mathbf{e}_\parallel$ by $\psi_\parallel$, with $\psi' = \psi - \psi_\parallel$, we then have

$$P_\psi\mathbf{e}_\perp = \sin(2\psi')\mathbf{e}_\parallel - \cos(2\psi')\mathbf{e}_\perp,$$

so we can express the components of the velocity $\mathbf{v}$ in (10) also as

$$v_\parallel - v_\mathrm{b} = R_\mathrm{b}[\cos\rho + \sinh\vartheta\,\sin(2\psi')\sin\rho],$$
$$v_\perp = R_\mathrm{b}\sin\rho[\cosh\vartheta + \sinh\vartheta\,\cos(2\psi')]. \tag{F1}$$

We can use this formula to determine the orientation of a low-symmetry skyrmion relative to the current for which the response velocity $\mathbf{v}$ has the largest component $v_\parallel$. This is interesting since the angle ψ can be changed by physically rotating a skyrmion. From (F1), we deduce that, for $Q > 0$, $v_\parallel$ is maximal when $\psi' = \pi/4$, while for $Q < 0$ it is maximal when $\psi' = 3\pi/4$.

The Sk Hall angle β, defined via $\tan\beta = v_\perp/v_\parallel$, can be calculated from (F1). Expressed in terms of the variables $\lambda_1, \lambda_2, \psi'$, which parametrize the shape of the skyrmion and its orientation, it is

$$\tan\beta = \frac{Q\big(\frac{1}{\xi} - \frac{1}{\alpha}\big)(\lambda_1\cos^2\psi' + \lambda_2\sin^2\psi')}{\lambda_1\lambda_2 + \frac{Q^2}{\alpha\xi} + (\lambda_2 - \lambda_1)Q\big(\frac{1}{\xi} - \frac{1}{\alpha}\big)\cos\psi'\sin\psi'}. \tag{F2}$$

This generalizes the result (12) for high-symmetry skyrmions given in the main text.

Finally, Eq. (F1) can be used to show that the response velocities of skyrmions with fixed $\vartheta > 0$ and ψ but different values of ρ necessarily lie on an ellipse. One checks that the velocity satisfies the equation of an ellipse,

$$(v_\parallel - v_\mathrm{b}, v_\perp)M\begin{pmatrix} v_\parallel - v_\mathrm{b} \\ v_\perp \end{pmatrix} = R_\mathrm{b}^2,$$

in terms of a symmetric and positive-definite matrix M which is determined by ϑ and ψ and is conveniently expressed in terms of its diagonal form as

$$M = R(\psi)\begin{pmatrix} \lambda_+ & 0 \\ 0 & \lambda_- \end{pmatrix}R(-\psi),$$

with eigenvalues proportional to those of Γ. In terms of the proportionality factor $\kappa = \lambda_1\cos^2\psi' + \lambda_2\sin^2\psi'$, they are

$$\lambda_+ = \lambda_1/\kappa, \quad \lambda_- = \lambda_2/\kappa.$$

The lengths of the major and minor axes are therefore

$$a = R_\mathrm{b}/\sqrt{\lambda_-}, \quad b = R_\mathrm{b}/\sqrt{\lambda_+}, \tag{F3}$$

giving the eccentricity

$$\varepsilon = \sqrt{\frac{a^2 - b^2}{a^2}} = \sqrt{\frac{\lambda_1 - \lambda_2}{\lambda_1}}. \tag{F4}$$

The directions of the axes of the ellipse are determined by the orthonormal basis, which also diagonalizes the dissipation tensor, namely,

$$\mathbf{e}_a = \begin{pmatrix} -\sin\psi \\ \cos\psi \end{pmatrix}, \quad \mathbf{e}_b = \begin{pmatrix} \cos\psi \\ \sin\psi \end{pmatrix}. \tag{F5}$$

Note that the major axis is in the direction of the eigenvector for the smaller eigenvalue. The ellipses with these axes and ellipse parameters (F3) all go through the points $(\alpha/\xi)\mathbf{e}_\parallel$ and $\mathbf{e}_\parallel$, as can also be seen from (F1).

We have seen that the apparently simple Thiele equation (4) captures surprising geometrical features of skyrmion dynamics. They are revealed by the general solution (10) and confirmed by numerical simulations. The geometrical features provide links to several themes in two-dimensional geometry even though the mathematics is superficially very different. The big circle of high-symmetry skyrmion velocities provides the most basic illustration of this point. The mapping of a line into a circle is a standard feature of Möbius transformations of the complex plane, and writing formula (10) for $Q \neq 0$ and $\vartheta = 0$ in terms of complex numbers gives just such a Möbius transformation of the scale parameter $\lambda = \lambda_1 = \lambda_2$. The small circles generated by varying ψ in (10) when $\vartheta > 0$ intersect the big circle at right angles. Circles with this property are geodesics in the Poincaré disk model of the hyperbolic plane. Identifying the boundary of the Poincaré disk with our big circle therefore leads to an unexpected connection between Thiele's equation (4) and hyperbolic geometry. As a final example of an unforeseen geometrical fact, the velocities of low-symmetry skyrmions (with $\vartheta \neq 0$) trace out an ellipse in velocity space when their overall scale is varied. Remarkably, this ellipse has the same eccentricity and orientation as the ellipse defined by the dispersion tensor Γ. While the big circle and the small circles can easily be seen in simulations of actual skyrmions and may be observable experimentally, the ellipses in velocity space are difficult to realize since they correspond to a special set of low-symmetry skyrmions whose dissipation tensors have a fixed rotation angle and eigenvalue ratio.

APPENDIX G: OTHER MAGNETIC SYSTEMS, INCLUDING CENTROSYMMETRIC ONES

Chiral magnets possess a lot of similarities with other magnetic materials, for example, frustrated magnets [44], hybrid systems [45–47] where chiral DMI accompanied by frustrated exchange interactions, and magnetic bubble materials [25] films of centrosymmetric magnets with strong easy-axis perpendicular anisotropy. Although the mechanism for stabilization of magnetic solitons in these systems is quite different, the ground state (spirals or stripe domains) and the behavior of the system in an external field (the transition to a skyrmion lattice or bubble domain lattice) are very similar. The analysis of Thiele's equation presented here is independent of the underlying 2D Hamiltonian. As a result, our classification of skyrmions into high symmetry, low symmetry, and topologically trivial can be applied to predict the dynamics of any magnetic soliton responding to a current through the Zhang-Li torque.

Accordingly, in all such systems, topological solitons with high symmetry have velocities lying on a circle, while topologically trivial solitons all have the same velocity $\mathbf{V}_0$. The theory developed here predicts similar properties for low-symmetry solitons in other magnetic systems. In particular, when the underlying Hamiltonian is degenerate with respect to rotations, we expect that spatially rotating low-symmetry solitons generates circles in the velocity plane, similar to those presented here for low-symmetry skyrmions in an isotropic chiral magnet. The size of these circles will be proportional to the difference in eigenvalues of the dissipation tensor, which is a measure of the soliton's elongation. Generally, stable configurations do not have strongly elongated shapes, so that their velocities lie close to the big circle (11). Therefore, we expect the velocity distribution to have the ringlike shape found here for most materials. Finally, we note that in the case of magnetic bubbles, three-dimensionality is crucial, and therefore, the theory proposed here may not cover cases where the magnetization is strongly inhomogeneous throughout the film thickness.

[1] T. H. R. Skyrme, A non-linear field theory, Proc. R. Soc. London, Ser. A **260**, 127 (1961).

[2] A. N. Bogdanov and D. A. Yablonskii, Thermodynamically stable "vortices" in magnetically ordered crystals. The mixed state of magnets, Sov. Phys. JETP **68**, 101 (1989).

[3] A. N. Bogdanov and A. Hubert, The properties of isolated magnetic vortices, Phys. Status Solidi B **186**, 527 (1994).

[4] A. N. Bogdanov and A. Hubert, Thermodynamically stable magnetic vortex states in magnetic crystals, J. Magn. Magn. Mater. **138**, 255 (1994).

[5] A. N. Bogdanov and A. Hubert, The stability of vortex-like structures in uniaxial ferromagnets, J. Magn. Magn. Mater. **195**, 182 (1999).

[6] See Supplemental Material at http://link.aps.org/supplemental/10.1103/PhysRevB.104.165116 for two movies showing the motion of skyrmions with $k_S = 1$, $Q = -1$ and antiskyrmions obtained in LLG simulations.

[7] F. N. Rybakov and N. S. Kiselev, Chiral magnetic skyrmions with arbitrary topological charge, Phys. Rev. B **99**, 064437 (2019).

[8] D. Foster, C. Kind, P. J. Ackerman, J.-S. B. Tai, M. R. Dennis, and I. I. Smalyukh, Two-dimensional skyrmion bags in liquid crystals and ferromagnets, Nat. Phys. **15**, 655 (2019).

[9] V. M. Kuchkin and N. S. Kiselev, Turning a chiral skyrmion inside out, Phys. Rev. B **101**, 064408 (2020).

[10] V. M. Kuchkin, B. Barton-Singer, F. N. Rybakov, S. Blügel, B. J. Schroers, and N. S. Kiselev, Magnetic skyrmions, chiral kinks and holomorphic functions, Phys. Rev. B **102**, 144422 (2020).

[11] B. Barton-Singer, C. Ross, and B. J. Schroers, Magnetic skyrmions at critical coupling, Commun. Math. Phys. **375**, 2259 (2020).

[12] C. Kind and D. Foster, Magnetic skyrmion binning, Phys. Rev. B **103**, L100413 (2021).

[13] Z. Zeng, C. Zhang, C. Jin, J. Wang, C. Song, Y. Ma, Q. Liu, and J. Wang, Dynamics of skyrmion bags driven by the spin–orbit torque, Appl. Phys. Lett. **117**, 172404 (2020).

[14] J. Tang, Y. Wu, W. Wang, L. Kong, B. Lv, W. Wei, J. Zang, M. Tian, and H. Du, Magnetic skyrmion bundles and their current-driven dynamics, Nat. Nanotechnol. (2021), doi:10.1038/s41565-021-00954-9.

[15] S. Zhang and Z. Li, Roles of Nonequilibrium Conduction Electrons on the Magnetization Dynamics of Ferromagnets, Phys. Rev. Lett. **93**, 127204 (2004).

[16] I. Dzyaloshinsky, A thermodynamic theory of "weak" ferromagnetism of antiferromagnetics, J. Phys. Chem. Solids **4**, 241 (1958).

[17] T. Moriya, Anisotropic superexchange interaction and weak ferromagnetism, Phys. Rev. **120**, 91 (1960).

[18] E. Davoli, G. Di Fratta, D. Praetorius, and M. Ruggeri, Micromagnetics of thin films in the presence of Dzyaloshinskii-Moriya interaction, arXiv:2010.15541.

[19] N. Romming, C. Hanneken, M. Menzel, J. E. Bickel, B. Wolter, K. Von Bergmann, A. Kubetzka, and R. Wiesendanger, Writing and deleting single magnetic skyrmions, Science **341**, 636 (2013).

[20] I. Kézsmárki, S. Bordács, P. Milde, E. Neuber, L. M. Eng, J. S. White, H. M. Rønnow, C. D. Dewhurst, M. Mochizuki, K. Yanai, H. Nakamura, D. Ehlers, V. Tsurkan, and A. Loidl, Néel-type skyrmion lattice with confined orientation in the polar magnetic semiconductor GaV_4S_8, Nat. Mater. **14**, 1116 (2015).

[21] N. Romming, A. Kubetzka, C. Hanneken, K. von Bergmann, and R. Wiesendanger, Field-Dependent Size and Shape of Single Magnetic Skyrmions, Phys. Rev. Lett. **114**, 177203 (2015).

[22] F. Jonietz, S. Mühlbauer, C. Pfleiderer, A. Neubauer, W. Münzer, A. Bauer, T. Adams, R. Georgii, P. Böni, R. A. Duine, K. Everschor, M. Garst, and A. Rosch, Spin transfer torques in MnSi at ultralow current densities, Science **330**, 1648 (2010).

[23] J. Zang, M. Mostovoy, J. H. Han and N. Nagaosa, Dynamics of Skyrmion Crystals in Metallic Thin Films, Phys. Rev. Lett. **107**, 136804 (2011).

[24] L. Kong and J. Zang, Dynamics of an Insulating Skyrmion under a Temperature Gradient, Phys. Rev. Lett. **111**, 067203 (2013).

[25] A. P. Malozemoff and J. C. Slonczewski, *Magnetic Domain Walls in Bubble Materials* (Academic, New York, 1979).

[26] L. D. Landau and E. M. Lifshitz, On the theory of the dispersion of magnetic permeability in ferromagnetic bodies, Phys. Z. Sowjetunion **8**, 153 (1935).

[27] Since $I = I(\xi)$, one should take into account that assuming that $I =$ const for varying ξ requires the current density $\mathbf{j}$ to change.

[28] A. A. Thiele, Steady-State Motion of Magnetic Domains, Phys. Rev. Lett. **30**, 230 (1973).

[29] S. Komineas and N. Papanicolaou, Skyrmion dynamics in chiral ferromagnets under spin-transfer torque, Phys. Rev. B **92**, 174405 (2015).

[30] To avoid ambiguity, in the definition of the topological charge (5) we follow the sign convention (see Ref. [48]) assuming that the skyrmion solutions always obey the condition $\mathbf{n}_0 = (0, 0, 1)$ for $|\mathbf{r}| \to \infty$.

[31] Note that the definition of the dissipation tensor in (6) up to the factor $4\pi\alpha$ is equivalent to the definition of "dissipation dyadic" provided in Ref. [25], Sec. VI.12 F.

[32] J. Masell, D. R. Rodrigues, B. F. McKeever, and K. Everschor-Sitte, Spin-transfer torque driven motion, deformation, and instabilities of magnetic skyrmions at high currents, Phys. Rev. B **101**, 214428 (2020).

[33] G. Malinowski, O. Boulle, and M. Kläui, Current-induced domain wall motion in nanoscale ferromagnetic elements, J. Phys. D **44**, 384005 (2011).

[34] M. Weißenhofer and U. Nowak, Orientation-dependent current-induced motion of skyrmions with various topologies, Phys. Rev. B **99**, 224430 (2019).

[35] A. Vansteenkiste, J. Leliaert, M. Dvornik, M. Helsen, F. Garcia-Sanchez, and B. Van Waeyenberge, The design and verification of MuMax3, AIP Adv. **4**, 10 (2014).

[36] M. J. Donahue and R. D. McMichael, Exchange energy representations in computational micromagnetics, Phys. B (Amsterdam, Neth.) **223**, 272 (1997).

[37] N. Papanicolaou and T. N. Tomaras, Dynamics of magnetic vortices, Nucl. Phys. B **360**, 425 (1991).

[38] A. M. Kosevich, B. A. Ivanov, and A. S. Kovalev, Magnetic solitons, Phys. Rep. **194**, 117 (1990).

[39] L. Bai and D. Breen, Calculating center of mass in an unbounded 2D environment, J. Graphics Tools **13**, 53 (2008).

[40] A. K. Nayak, V. Kumar, T. Ma, P. Werner, E. Pippel, R. Sahoo, F. Damay, U. K. Rößler, C. Felser, and S. S. P. Parkin, Magnetic antiskyrmions above room temperature in tetragonal Heusler materials, Nature (London) **548**, 561 (2017).

[41] J. Wang, J. Xia, X. Zhang, X. Zheng, G. Li, L. Chen, Y. Zhou, J. Wu, H. Yin, R. Chantrell, and Y. Xu, Magnetic skyrmionium diode with a magnetic anisotropy voltage gating, Appl. Phys. Lett. **117**, 202401 (2020).

[42] Y. Ishida and K. Kondo, Theoretical comparison between skyrmion and skyrmionium motions for spintronics applications, Jpn. J. Appl. Phys. **59**, SGGI04 (2020).

[43] N. Sisodia, P. K. Muduli, N. Papanicolaou, and S. Komineas, Chiral droplets and current-driven motion in ferromagnets, Phys. Rev. B **103**, 024431 (2021).

[44] A. O. Leonov and M. Mostovoy, Multiply periodic states and isolated skyrmions in an anisotropic frustrated magnet, Nat. Commun. **6**, 8275 (2015).

[45] L. Rózsa, A. Deák, E. Simon, R. Yanes, L. Udvardi, L. Szunyogh, and U. Nowak, Skyrmions with Attractive Interactions in an Ultrathin Magnetic Film, Phys. Rev. Lett. **117**, 157205 (2016).

[46] A. K. Nandy, N. S. Kiselev, and S. Blügel, Interlayer Exchange Coupling: A General Scheme Turning Chiral Magnets into Magnetic Multilayers Carrying Atomic-Scale Skyrmions, Phys. Rev. Lett. **116**, 177202 (2016).

[47] U. Ritzmann, S. von Malottki, J.-V. Kim, S. Heinze, J. Sinova, and B. Dupé, Trochoidal motion and pair generation in skyrmion and antiskyrmion dynamics under spin–orbit torques, Nat. Electron. **1**, 451 (2018).

[48] C. Melcher, Chiral skyrmions in the plane, Proc. R. Soc. A **470**, 20140394 (2014).